Solar Phys (2008) 250: 53–73
DOI 10.1007/s11207-008-9193-9

A Statistical Survey of Hard X-ray Spectral Characteristics of Solar Flares with Two Footpoints

P. Saint-Hilaire · S. Krucker · R.P. Lin

Received: 31 July 2007 / Accepted: 22 April 2008 / Published online: 30 May 2008

Abstract Using RHESSI data, we have analyzed 172 hard X-ray (HXR) peaks during 53 solar flares that exhibited a double-footpoint structure. Fitting both footpoints with power laws, we find that spectral index differences $\Delta\gamma$ range mostly between 0 to 0.6, and only rarely go beyond. Asymmetries between footpoints were not observed to be significantly dependent on their mean heliographic position, their relative position with respect to each other, nor their orientation with respect to the solar equator. By assuming a symmetric acceleration process, it is also clear that differences in footpoint spectral indices and footpoint flux ratios can seldom be attributed to a difference in column densities between the two legs of a coronal loop. Our results corroborate better the magnetic mirror trap scenario. Moreover, footpoint asymmetries are more marked during times of peak HXR flux than when averaging over the whole HXR burst, suggesting that the magnetic configuration evolves during individual HXR bursts. We also observed a linear correlation between the peak 50-keV flux and the peak GOES 1 – 8 Å channel flux and that HXR burst duration seem correlated with loop length.

Keywords Flare, spectrum · X-ray bursts, spectrum · Footpoint

1. Introduction

Solar flares are believed to be powered by magnetic reconnection high in the corona, which accelerates particles. Particles, and in particular electrons, travel down field lines and emit bremsstrahlung hard X-rays (HXR) as they penetrate the denser chromosphere. Hence the HXR radiation from the footpoints contains much information about the accelerated electrons (though convoluted with transport effects), such as energy content (Brown, 1971; Holman *et al.*, 2003; Saint-Hilaire and Benz, 2005).

P. Saint-Hilaire (✉) · S. Krucker · R.P. Lin
Space Sciences Laboratory, University of California, Berkeley, CA 94720, USA
e-mail: shilaire@ssl.berkeley.edu

S. Krucker
e-mail: krucker@ssl.berkeley.edu

The first observations of HXR footpoints were made by Hoyng *et al.* (1981) on SMM. *Yohkoh* HXT later characterized the "standard" flare model: two footpoints and an above-the-looptop source (Masuda, 1994). The above-the-looptop source is rarely observed, although that could be due to observational constraints.

Statistical studies of HXR footpoints (and looptop) sources' spectral indices using the *Yohkoh* satellite (Sakao, 1994; Petrosian, Donaghy, and McTiernan, 2002) have been carried out in the past. Some of their results seem to indicate that the spectral indices of two neighboring footpoints could differ by as much as 1 or even 2! Such differences cannot be explained easily by transport mechanisms (see, *e.g.,* Appendix A). *Yohkoh* HXT's results were compromised by the fact that it had only had four energy channels and had to deal with issues such as thermal contamination of the lowest channel(s) and the sometime poor statistics of the upper ones.

The Ramaty High Energy Solar Spectroscopic Imager (RHESSI, Lin *et al.*, 2002) offers an unprecedented combination of spectral resolution (1 keV in the 3 – 100 keV range), spatial resolution (2.3″), temporal evolution (≈ 2 s), and sensitivity comparable to *Yohkoh* HXT's. Previous RHESSI imaging spectroscopy results include those of Krucker and Lin (2002), Emslie *et al.* (2003), and Battaglia and Benz (2006). A similar time variation of spectra in footpoints is observed, although in some cases, the spectrum in one footpoint is steeper than in the other one (by about 0.3 in spectral index in Emslie *et al.*, 2003). Emslie *et al.* (2003) suggest that the discrepancy could be due to a difference in column densities of the electron population, as they propagate down an asymmetric loop (*cf.* Appendix A).

All RHESSI papers to date discuss only a single event, or a few events, but no statistical study of the footpoints has been done so far that exploit RHESSI's large database of observed flares. These results should help constrain energy release and particle acceleration in the flare model.

2. Event Selection

RHESSI has been in orbit for six years now. Since its launch on 5 February 2002, it has observed more than 20 000 flares. For this study, the strongest flares will be taken into considerations, as they have better count statistics. More specifically, we select flares that show substantial emission above 50 keV (where solar flare thermal components are always negligible), enough to produce images of good enough quality to be used in imaging spectroscopy (2000 counts is about the minimum for a reliable single-image reconstruction with two sources). To achieve our objectives, we will use the simplest possible events, those that show only two footpoints.

The HESSI Experimental Data Center (HEDC; Saint-Hilaire and Benz, 2002) was used to find our events. The database was queried for all flares between 13 February 2002 and 1 July 2006 that had two or more sources and peak GOES flux above M1.0 level. More than 1100 flares corresponded to that description. Each was individually examined, in particular by looking at the time versus energy panels of RHESSI images that HEDC automatically produces for each flare (one-minute accumulations over whole-flare duration). The flares that were retained were those that visually displayed two footpoints in HEDC images above 50 keV. A total of 53 flares were kept (see Table 1).

3. Method of Analysis

Imaging spectroscopy using CLEAN (Hurford *et al.*, 2002) and the OSPEX spectral analysis software was employed. Imaging was done by using collimators 3 to 8, yielding a formal

Table 1 Flares studied, GOES X-ray class, and position on the Sun in both arcseconds from Sun center and heliographic coordinates.

Flare number	Date and time	GOES class	Location on Sun		
			X [″]	Y [″]	Latitude/Longitude
1	2002/02/20 11:06:12	C7.5	904.4	261.5	N13 W73
2	2002/03/17 10:15:36	M1.4	−342.2	−239.2	S20 E22
3	2002/03/17 19:28:44	M4.4	−264.8	−232.9	S20 E17
4	2002/04/10 12:28:04	M8.8	−20.8	434.5	N20 E01
5	2002/04/10 19:02:48	M1.8	−348.2	377.5	N17 E22
6	2002/05/31 00:07:08	M2.4	−817.5	−475.4	S30 E87
7	2002/06/01 03:53:40	M1.6	−414.8	−293.0	S18 E27
8	2002/06/02 11:44:32	M1.0	−148.8	−300.3	S18 E09
9	2002/07/17 07:02:48	M9.2	288.5	246.5	N19 W18
10	2002/07/18 03:32:56	M2.5	421.4	264.5	N20 W28
11	2002/07/23 00:28:04	X5.1	−868.1	−235.3	S12 E70
12	2002/07/29 10:39:08	M5.1	238.9	−291.3	S12 W14
13	2002/07/31 01:48:40	M1.4	558.4	−220.2	S08 W36
14	2002/08/03 19:04:36	X1.2	899.8	−265.8	S15 W80
15	2002/08/21 01:39:16	M1.6	689.2	−246.7	S10 W47
16	2002/08/22 01:52:00	M5.9	798.4	−266.5	S12 W59
17	2002/09/08 01:39:08	M1.6	−908.8	−193.1	S09 E75
18	2002/09/27 03:34:28	M1.0	−694.7	142.9	N13 E47
19	2002/12/04 22:47:00	M2.5	−836.7	227.7	N13 E61
20	2003/04/23 01:01:56	M5.1	261.8	366.8	N17 W16
21	2003/05/29 01:04:40	X1.2	494.4	−106.6	S07 W31
22	2003/06/17 22:53:40	M6.8	−790.4	−138.6	S07 E57
23	2003/07/17 08:19:46	C9.7	−206.9	178.2	N15 E13
24	2003/10/23 08:47:20	X5.4	−904.8	−317.4	S18 E81
25	2003/10/24 02:48:32	M7.7	−865.1	−341.1	S19 E71
26	2003/10/29 20:43:20	X10	90.8	−381.3	S18 W05
27	2003/11/01 22:33:04	M3.3	818.6	−253.8	S13 W60
28	2003/11/03 09:49:16	X3.9	917.8	130.3	N08 W73
29	2003/11/04 19:33:56	M9.1	900.8	−335.0	S19 W81
30	2004/01/06 06:22:32	M2.7	−972.6	88.3	N05 E89
31	2004/01/07 10:22:12	M3.7	−930.2	117.0	N05 E73
32	2004/04/06 13:22:48	M2.3	−261.5	−170.6	S16 E16
33	2004/07/13 00:15:26	M6.8	654.7	181.6	N14 W45
34	2004/07/23 21:19:28	M1.8	125.5	6.6	N05 W07
35	2004/09/12 00:33:44	M4.8	−706.2	−35.9	N02 E47
36	2004/10/30 03:30:09	M3.5	316.8	145.2	N12 W19
37	2004/10/30 16:24:26	M6.0	427.6	139.5	N12 W26
38	2004/10/31 05:32:03	M2.4	540.6	152.6	N12 W34
39	2004/11/03 03:30:52	M1.6	−674.1	94.7	N08 E44
40	2004/11/06 00:30:48	M9.5	−79.3	83.4	N08 E04

Table 1 (*Continued*)

Flare number	Date and time	GOES class	Location on Sun		
			X [″]	Y [″]	Latitude/Longitude
41	2004/11/06 01:42:34	M3.7	−27.4	68.1	N07 E01
42	2004/11/10 02:09:44	X2.6	700.1	91.4	N07 W46
43	2004/12/01 07:10:16	M1.2	−335.8	128.5	N08 E20
44	2005/01/15 06:28:31	M8.4	−106.1	295.5	N12 E06
45	2005/01/15 22:48:24	X2.7	103.1	306.7	N13 W06
46	2005/01/17 10:00:23	X3.9	430.0	292.3	N13 W26
47	2005/01/19 08:12:40	M8.7	708.9	283.6	N13 W48
48	2005/01/19 10:21:08	M2.5	679.6	339.9	N16 W46
49	2005/01/20 06:44:44	X7.1	818.5	256.0	N12 W59
50	2005/07/13 14:14:14	M2.7	909.4	168.9	N11 W78
51	2005/08/22 01:11:54	M2.3	717.8	−248.7	S10 W50
52	2005/08/22 17:07:34	M5.2	801.4	−241.6	S11 W59
53	2005/08/23 14:46:21	M2.7	883.8	−219.0	S11 W71

image resolution of 7″ FWHM. The time intervals and energy intervals were chosen as follows.

For each flare, two types of time intervals were used:

- *"Peak flux" time intervals:* These are four RHESSI spin periods long (with each RHESSI spin period being about 4 s long), centered at the time of peak HXR (above 50 keV) flux. The later is found by using RHESSI Observing Summary data (Schwartz *et al.*, 2002). The peak flux time interval was taken to be this time of peak flux plus or minus two RHESSI spin periods (which are $\approx$4 s long). Of course, there can be only one such peak flux time interval per flare, resulting in 53 such peaks in our study. If we take the flare of 13 July 2005 as an example (Figure 1), the time interval of accumulation was about 14:14:05 to 14:14:22.
- *"Whole peak" time intervals:* Strong nonthermal peaks appearing in RHESSI spectrograms (or dynamic spectra) were selected over their whole *time interval*, defined as the time the HXR flux ($>$ 50 keV) is greater than 50% of its peak value. There can be many such "whole peak" time intervals within the same flare. And of course, for each flare, one of the "whole peak" time interval envelops that flare's "peak flux" time interval. Again if we take the flare of 13 July 2005 as an example (Figure 1), the time intervals of accumulation were about 14:13:47 to 14:19:50, and 14:21:22 to 14:24:41. In a few cases, time intervals did not contain two footpoints (but only one, or sometimes three or more) and were hence discarded from the study.

For each time interval, the energy binning was chosen by using the following semi-empirical approach:

- The *start* (*lowest*) energy was visually chosen by inspection of the RHESSI spectrogram: It is taken to be the point where the nonthermal emission starts to be clearly stronger than the thermal component.
- The energy binning was taken to be pseudo-logarithmic, with each energy bin having at least 2000 counts above background, and the bin width being between 5% and 20% of the bin value. This was crudely approximated by using Observing Summary 4 second

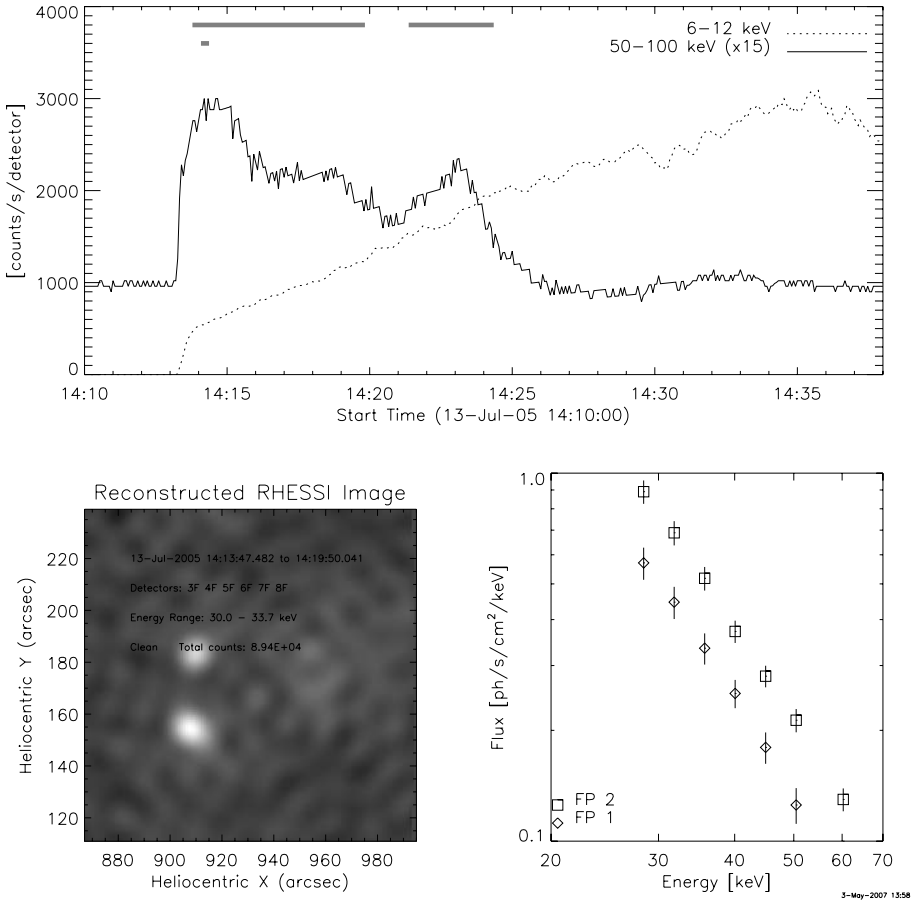

Figure 1 RHESSI time profile (top), 30 – 33 keV image (bottom left), and footpoint spectra (bottom right) of the 13 July 2005 M2.7 flare. The gray bars represent the time intervals chosen for our analysis: a "Peak Time" 16-second interval around 14:14:10 and two "Whole Peaks," from 14:13:47 to 14:19:50 and from 14:21:22 to 14:24:41. The third HXR peak (≈14:30) was discarded as it was faint, and there was an attenuator state change (Lin *et al.*, 2002) during it, further complicating the analysis. The Sun was eclipsed by the Earth until ≈ 14:13.

data rates. The *end* (*highest*) energy was taken to be when the next energy bin could not achieve 2000 counts above background. We had 4 to 18 (typically 10) energy bins with which to fit and obtain spectral indices and fluxes.

Finally, for the results presented and discussed in this paper, only fittings deemed "most reliable" were kept. "Most reliable" meant those that had at least six or more energy bins for footpoint spectral fitting with a best-fit χ^2 value of 5 or less. Ultimately, 33 "Peak Time" and 89 "Whole Peaks" events were used to produce the results that we analyze here.

To limit *pulse pileup* issues (Smith *et al.*, 2002), care has been taken to discard times with high count rates (*i.e.*, just before shutters moving in). Moreover, as spectral fitting was usually done above 25 keV, only times with very strong emission (during which both attenuators are in "A3" state) can potentially produce an additional component around 35 keV (with only the thin shutter in "A1" state), with detector count rates peaking around 12 keV,

Table 2 Measured and derived quantities.

Symbol	Name or description
γ_1, γ_2	Spectral indices of both footpoints, as obtained by fitting a power law by using the OSPEX from the *Solarsoft* suite of routines
$\Delta\gamma$	Spectral index difference $\Delta\gamma = \gamma_1 - \gamma_2$ between footpoints
$\bar{\gamma}$	$=\frac{1}{2}(\gamma_1 + \gamma_2)$: average spectral index
$F_{50,1}$, $F_{50,2}$	50-keV photon flux in both footpoints [s^{-1} cm^{-2} keV^{-1}]
$F_{50,\mathrm{tot}}$	$=F_{50,1} + F_{50,2}$, total flux
$F_{50,\mathrm{r}}$	$=\frac{F_{50,1}}{F_{50,2}}$: 50-keV flux ratio between footpoints
dt	Duration or accumulation time [s]
GOES	GOES X-ray class, or flux [W m^{-2}] in the low 1 – 8 Å channel
Lat_1, Lat_2	Heliographic longitude [degrees] of both footpoints. The footpoint with the largest longitude (or "leading") is labeled "1"; the other one "2"
Lon_1, Lon_2	Heliographic latitude of both footpoints [degrees]
s	Spherical separation between footpoints [Mm]
α	Angle between footpoints and solar equator

and these can be piled up to ≈ 24 keV. In A3 state, the peak of the response is around ≈ 18 keV counts. These photons can pile up and appear as ≈ 36 keV photons. In 20 of our events the contribution of pile-up photons in certain energy channels was larger than 15%. As pileup typically makes two thermal photons appear as a single higher energy photon, imaging piled-up photons would place them at the location of the thermal source. In 19 of these 20 cases, the thermal source was spatially distinct from the HXR footpoints, thereby little influencing our results. In the remaining case, the thermal source overlapped with the nonthermal HXR footpoints (within our $7''$ spatial resolution), and spectral fitting was done above 40 keV to eliminate any contamination by piled-up low-energy photons.

Table 2 is a list of all parameters obtained for each of our events. Subscripts 1 and 2 refer to the value of the leading and trailing footpoints, respectively (as determined by their heliographic longitude). In a few cases, the subscripts *strong* and *weak* were also used. They refer to the value of the strongest and weakest footpoints, respectively (as determined by their 50-keV flux).

Presenting all possible combination of scatter plots is prohibitive (but they can be found at a Web site[1]). Only the most relevant have been presented, but all have of course been examined, and an exhaustive table of computed correlation coefficients can be found in Section 4.3.

[1] http://sprg.ssl.berkeley.edu/~shilaire/FootPointProject/htmlsummaries/browser.html.

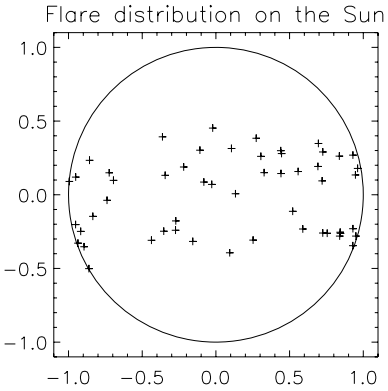

Figure 2 Distribution of our sample of 53 flares on the Sun.

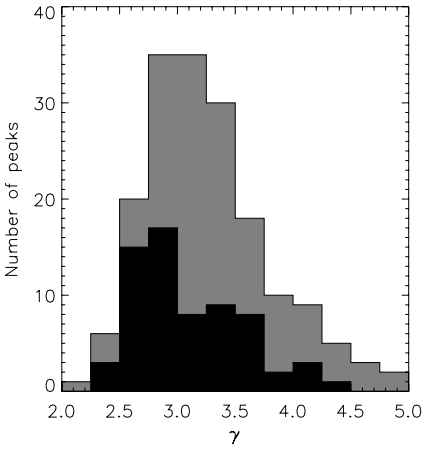

Figure 3 Histogram of spectral indices γ. The gray bars are for "Whole Peaks" events; the black ones are for "Peak Time" events. The bin size (0.2) was taken to be larger than the average error of 0.16.

4. Observations and Discussion

4.1. Spatial Information

Figure 2 shows the spatial distribution of our 53 flares on the Sun. As already known, flares occur predominantly at ± 15 degrees of latitude, and there is no marked longitudinal dependence. The slight lack of events at high longitudes is very probably due to observational bias: With our imaging method (CLEAN with detectors 3 and above), flares with footpoint separation smaller than $\approx 10''$ appear to be single-footpoint flares and are not selected. Projection effects near the solar limb reduce the apparent footpoint separation, causing some of these flares to be discarded.

4.2. Spectral Information

Figure 3 shows that spectral indices are generally harder for "Peak Time" events, which is of course no surprise, as it is a natural consequence of the soft – hard – soft behavior observed in a majority of flares, where the flattest spectral index corresponds to the time of most intense HXR emission (see, *e.g.,* Grigis and Benz, 2004). Flares are very seldom harder than $\gamma \approx 2.4$ in photon spectral index [see, *e.g.*, Kašparová *et al.* (2005) and references therein].

Table 3 Consistency/inconsistency of $\Delta\gamma$ with zero: The numbers on the left of the "|" are the number of cases where $\Delta\gamma - n \cdot \sigma_{\Delta\gamma} > 0$, and numbers on the right are events where $\Delta\gamma + n \cdot \sigma_{\Delta\gamma} < 0$. The total number of each type of event is given in parentheses at the top of each column.

Event type	"Peak Times" (33 events)	"Whole Peaks" (87 events)	Main "Whole Peak" of each flare (37 events)
$n = 0$	17|16	54|33	21|16
$n = 1$, "1-sigma results"	10|15	34|19	12|11
$n = 2$, "2-sigma results"	5|4	16|8	6|4
$n = 3$, "3-sigma results"	2|1	5|2	1|0

Table 4 Consistency/inconsistency of $F_{\rm r}$ with unity: Events with $F_{\rm r} - n \cdot \sigma_{F_{\rm r}} > 1$ are left of the "|", and events with $F_{\rm r} + n \cdot \sigma_{F_{\rm r}} < 1$ are at the right.

Event type	"Peak Times" (33 events)	"Whole Peaks" (87 events)	Main "Whole Peak" of each flare (37 events)
$n = 0$	20|13	41|46	21|16
$n = 1$, "1-sigma results"	20|13	40|39	21|15
$n = 2$, "2-sigma results"	19|12	32|34	16|13
$n = 3$, "3-sigma results"	19|11	24|32	12|12

The distribution at high γ in Figure 3 is not to be trusted, as it is distorted by observational bias: Only flares with sufficient HXR emission above 50 keV (*i.e.*, flares with hard spectra) were used in our study.

Another observational constraint is the instrument's dynamic range *DR*: The weakest footpoint is visible if $F_{\rm weak} \geq \frac{F_{\rm strong}}{DR}$. Given a conservative dynamic range of ≈ 5 for RHESSI, this means that if a footpoint is weaker than the other one by a factor 5 or more, it will not be imaged.

Figure 4 displays scatter plots of the average spectral indices ($\bar{\gamma}$) or spectral index differences ($\Delta\gamma$) versus the total 50-keV flux ($F_{50,\rm tot}$) or the 50-keV flux ratio ($F_{50,\rm r}$) of our events, with error bars. And, indeed, no event shows a flux ratio greater than 5 (or smaller than 0.2). Very few footpoint pairs have spectral index difference greater than 0.6, and none above 0.8. This fact could not be attributed to observational effects. During our data reduction, a few events with $\Delta\gamma$ larger than 1 were found, but they were discarded because of poor statistics (large χ^2 fitting parameter) and/or the appearance of a third source.

Roughly 25% of "Peak Time" events (8 out of 33) have spectral index differences consistent with zero (*i.e.*, $\Delta\gamma$ within 1σ of zero; Table 3). This ratio increases to $\approx 40\%$ for "Whole Peak" events (34/87).

No "Peak Time" event (0/33, Table 4) has a flux ratio consistent with unity, and only $\approx 10\%$ of the "Whole Peak" events do (8/87; this fraction is almost reduced to zero (1/37) when the strongest "Whole Peak" events of each flare is considered (*i.e.,* those encompassing the "Peak Time")]. Table 4 seem to suggest that leading footpoints might have more flux during "Peak Time" events, but the result is not statistically significant and will not be further discussed.

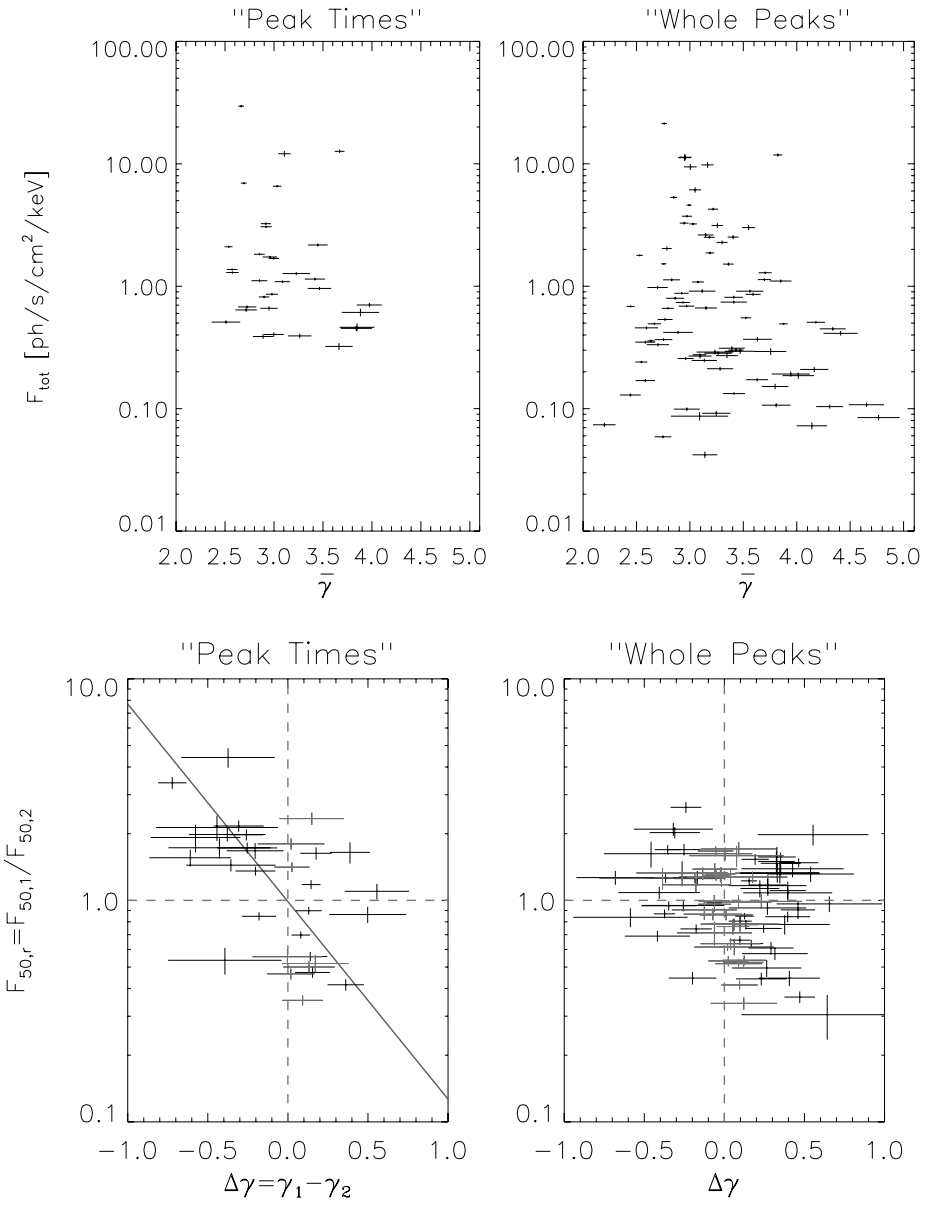

Figure 4 Top: $\bar{\gamma}$ versus $F_{50,\mathrm{tot}}$, with 1-σ error bars. Bottom: $\Delta\gamma$ and $|\Delta\gamma|$ versus $F_{50,\mathrm{r}}$, with 1-σ error bars (see Table 2 for an explanation of all quantities). The data points in gray are the ones for which $|\Delta\gamma| < \sigma_{\Delta\gamma}$. The thick gray line is a linear regression to the $\Delta\gamma$ versus $F_{50,\mathrm{r}}$ "Peak Time" data.

Figure 5 and Table 3 show that there is no statistically significant preference for the leading footpoint to be either harder or softer than the trailing one, during either "Peak Times" or "Whole Peaks."

The deficit of $F_{50,\mathrm{r}} \approx 1$ events during "Peak Times" is particularly clear in Figures 4 (bottom left) and 6 (which show only 1 out of 33 events within 10% of unity flux ratio, and

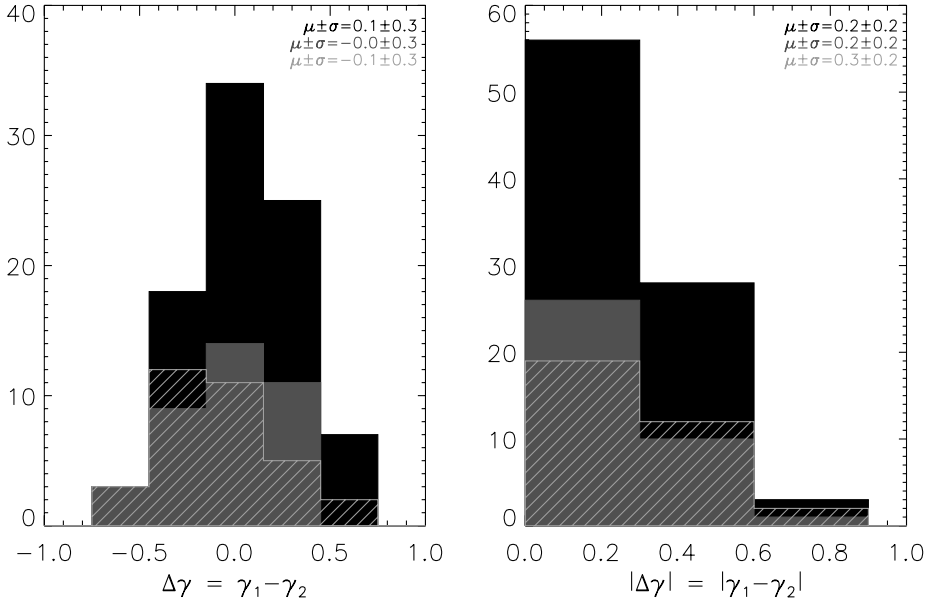

Figure 5 Histogram of spectral index differences $\Delta\gamma$ showing "Peak Time" events (cross-hatched), "Whole Peak" events (solid black), and "Whole Peak" events (solid gray; only one per flare, the one overlapping the peak HXR flux time). The bin size (0.3) was taken larger than the average error (0.23).

Table 5 Column density model: (agreement/disagreement).

Event type	"Peak Times"	"Whole Peaks"	All together
All events	30.3% (10/33)	39.1% (34/87)	36.7% (44/120)
1-sigma results	24% (6/25)	42.9% (21/49)	36.5% (27/74)
2-sigma results	28.6% (2/7)	40.0% (8/20)	37.0% (10/27)
3-sigma results	33% (1/3)	60.0% (3/5)	50.0% (4/8)

only 5 out of 33 within 20%). This greater footpoint asymmetry during times of peak HXR fluxes than during whole HXR peaks could indicate that individual particle acceleration episodes occur preferentially in one direction of the loop at any given time, but that, on the average, particles tend to be accelerated in both directions equally.

We checked in a simple way the agreement of our data set with the theory presented in Appendix A: that spectral index differences $\Delta\gamma$ between flare footpoints might be due to differences in column depths in asymmetric loops. This effect, under the assumption of equal distributions of electrons accelerated in both directions of the loop, results in the footpoint having the softer spectrum and also having the most flux. As shown in Figure 7 and Table 5, the reverse happens most of the time, better supporting a "magnetic mirroring" type of effect [see, *e.g.,* recent work by Schmahl *et al.* (2007) and references therein]. Furthermore, the best candidate in support of the column density difference model, the 23 July 2002 flare (which agrees at the "3-σ level"), actually hits a snag when one considers the amount of 50-keV flux (predicted by theory) out of the footpoints (*i.e.*, emitted somewhere along the legs of the loop, before reaching the imaged footpoints): As explained in Appendix A, this 50-keV emission should have been observable. Moreover, the presence of large flux ratios F_r

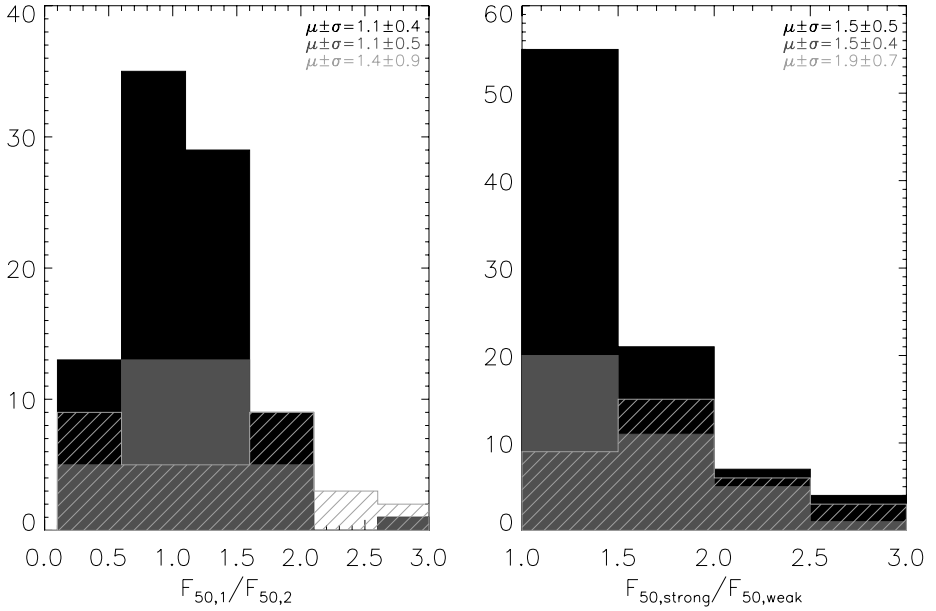

Figure 6 Histogram of flux ratios showing "Peak Time" events (cross-hatched), "Whole Peak" events (solid black), and "Whole Peak" events (solid gray; only one per flare, the one overlapping the peak HXR flux time). The bin size (0.5) is much larger than the typical error.

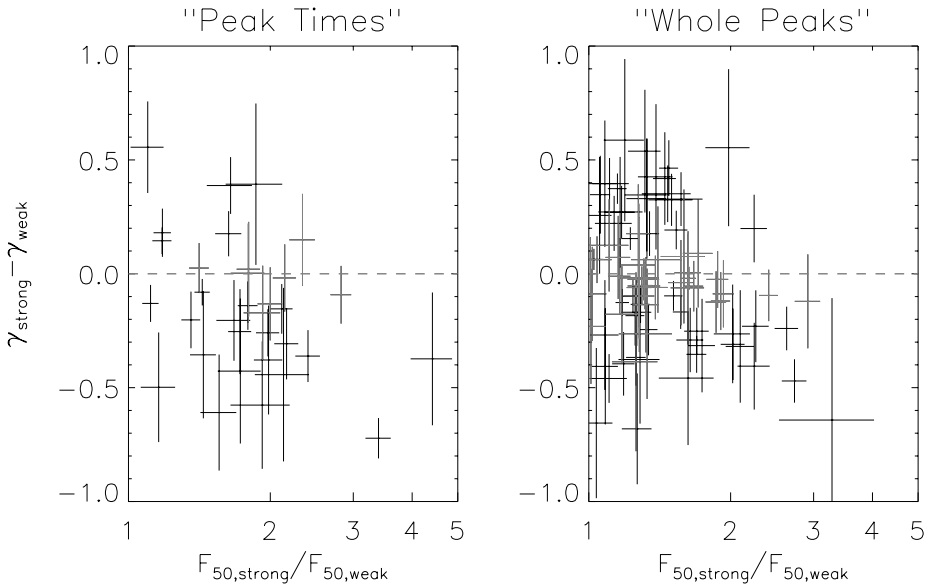

Figure 7 $F_{50,\mathrm{strong}}/F_{50,\mathrm{weak}}$ versus $\gamma_{\mathrm{strong}} - \gamma_{\mathrm{weak}}$, where strong (weak) denotes the footpoint with the strongest (weakest) 50-keV flux, respectively. The dashed line marks zero spectral index difference. There are 23 out of 33 (79%) "Peak Flux" events and 53 out of 87 (61%) "Whole Peak" events that lie below the dashed line (see also Table 5).

(2 or above, $\frac{1}{2}$ or below) also leads us to believe that this theory cannot be a dominant factor, at least for reasonable values of leg column densities (see Appendix A).

There are several alternatives to explain footpoint asymmetries: (a) *asymmetrical acceleration*, (b) *nonuniform target ionization*, and (c) *magnetic mirroring*. (a) The strong footpoint asymmetries, particularly during HXR peak times, suggest that it is the acceleration mechanism itself that could be asymmetrical. If the acceleration process actually took place in the chromospheric footpoints (as opposed to high in the corona), one would expect asymmetries, as both acceleration processes could in principle be independent of one another. (b) It is conceivable that the two chromospheric footpoints have different ionization structure; for example, consider the simplified step model of Brown (1973) or Kontar, Brown, and McArthur (2002), in which the column density required before reaching the lower chromospheric regions of neutral atoms is different in the two legs of the loop, perhaps owing to some prior heating of only one of the footpoints. Modeling and comparison with observations are required to further this idea. (c) The best candidate mechanism to explain footpoint emission asymmetries is magnetic mirroring, as discussed in the *trap+precipitation* model (Melrose and Brown, 1976) of Aschwanden *et al.* (1999), in which the magnetic field converges more rapidly in one of the footpoints, and particles are mirrored before they reach the dense lower regions (see also Schmahl *et al.*, 2007). Our data better corroborate that scenario than the column density asymmetry model. The effects of *photospheric albedo* (Bai and Ramaty, 1978) or *return currents* (Zharkova and Gordovskyy, 2006) might reinforce any asymmetry observed in footpoint photon spectra, but only if the accelerated electron distributions started out different.

4.3. Correlation Table

Correlation coefficients have been computed for our data and are displayed in Table 6.

We found the following:

- There is some degree of anticorrelation (-0.53, with the 95% confidence interval being $[-0.74, -0.22]$) between $\Delta\gamma$ and F_{r}, for "Peak Time" events. This is a consequence of there having more events in the upper left and lower right quadrants of the lower left panel of Figure 4 and has already been discussed in Section 4.2.
- $\bar{\gamma}$ and $|\Delta\gamma|$ seem also slightly correlated, indicating that $|\Delta\gamma|$ is larger when the flare is softer. Upon closer examination, it appears that softer spectra simply have larger errors.
- An unexpected correlation – albeit weak (with a 95% confidence interval of [0.32, 0.67]) – was found between footpoint separation and event duration for "Whole Peak" events.

  From Figure 8, it seems that we have

$$(\text{HXR burst duration}) \approx (\text{footpoint separation})^2, \tag{1}$$

  or, by assuming semicircular loops,

$$(\text{HXR burst duration}) \approx (\text{loop length})^2. \tag{2}$$

  It seems that the longer the loops, the longer the HXR peak will last. The interpretation is not yet clear. It could be a simple case of larger loops needing more time to evolve than the short ones during the flaring process or another case of the "big flare syndrome": Everything is bigger in larger flares.
- There is excellent correlation between "Peak Time" total flux and GOES class (with a 95% confidence interval for the correlation coefficient of 0.77 – 0.94), but the correlation is poorer for "Whole Peaks" total flux and GOES class (with a 95% confidence interval for the correlation coefficient of 0.57 – 0.81).

Table 6 Table of correlation coefficients between footpoint parameters: Where there are two numbers separated by a slash, the number to the left applies to "Peak Times" and the one to the right applies to "Whole Peaks." Correlation coefficients with magnitude greater than 0.5 are in bold.

	Duration [s]	50-keV flux ratio $\ln(\frac{F_{50,1}}{F_{50,2}})$	50-keV flux $\ln(F_{50,1}+F_{50,2})$	$\Delta\gamma$	$\lvert\Delta\gamma\rvert$	$\bar{\gamma}$
Duration [s]	−/1.00	−/−0.08	−/−0.01	−/−0.07	−/−0.11	−/−0.21
$\ln(\frac{F_{50,1}}{F_{50,2}})$		1.00/1.00	0.06/0.12	−0.53/−0.23	0.45/0.09	0.32/0.22
$\ln(F_{50,1}+F_{50,2})$			1.00/1.00	0.24/0.11	−0.22/−0.13	−0.23/−0.24
$\Delta\gamma$				1.00/1.00	−0.42/0.16	−0.41/−0.08
$\lvert\Delta\gamma\rvert$					1.00/1.00	**0.50**/0.49
$\bar{\gamma}$						1.00/1.00
Longitude						
|Longitude|						
Latitude						
|Latitude|						
FP separation						
FP angle						
ln(GOESflux)						

Table 6 (*Continued*)

	Longitude	|Longitude|	Latitude	|Latitude|	FP separation	FP angle	GOES class
Duration [s]	−/0.02	−/−0.08	−/−0.03	−/0.10	**−/0.52**	−/−0.05	−/0.22
$\ln\left(\frac{F_{50,1}}{F_{50,2}}\right)$	0.15/0.05	−0.24/−0.12	−0.01/0.07	0.43/0.10	−0.12/−0.07	−0.07/0.01	0.16/0.12
$\ln(F_{50,1}+F_{50,2})$	0.26/−0.06	0.12/0.17	0.20/0.01	−0.25/−0.14	0.04/0.00	0.22/0.20	**0.88/0.71**
$\Delta\gamma$	−0.01/−0.08	0.33/0.31	−0.20/−0.19	−0.12/−0.18	−0.18/−0.03	0.05/0.25	0.11/0.03
$\lvert\Delta\gamma\rvert$	−0.01/−0.02	−0.25/0.12	0.12/−0.20	0.19/0.13	0.01/−0.18	−0.04/0.08	−0.09/−0.07
$\bar{\gamma}$	0.29/0.31	−0.24/−0.16	0.06/−0.03	−0.06/0.11	−0.01/−0.42	−0.26/−0.02	−0.12/−0.22
Longitude	1.00	−0.04	0.17	−0.06	−0.02	0.09	0.12
|Longitude|		1.00	−0.27	−0.08	0.13	0.13	0.07
Latitude			1.00	−0.27	−0.08	0.25	−0.03
|Latitude|				1.00	−0.18	−0.12	0.02
FP separation					1.00	−0.15	0.22
FP angle						1.00	0.13
ln(GOES flux)							1.00

Figure 9 shows the clear correlation between an event's maximum GOES 1 – 8 Å flux and the total HXR flux F_{50}, for "Peak Time" events. Fitting a power law yields

$$F_{50} = A \cdot F^{\alpha}_{\text{GOES, 1–8 Å}}, \tag{3}$$

where $A = (4.7 \pm 0.3) \times 10^3$ and $\alpha = 0.8 \pm 0.1$ when F_{50} is in photons $\text{s}^{-1}\,\text{cm}^{-2}\,\text{keV}^{-1}$ and $F_{\text{GOES, 1–8 Å}}$ in $\text{W}\,\text{m}^{-2}$. The *bisector* method (Isobe *et al.*, 1990) is more relevant when the variables are independent, in which case we have $A = 10^{4.3\pm0.2}$ and $\alpha = 0.97 \pm 0.05$. (Of course, "Whole HXR Peaks" events typically lie below this solid line, with a wide scatter.)

This good correlation can be interpreted as a direct consequence of the Neupert effect (Neupert, 1968; Dennis, 1985): the larger the amount of nonthermal energy (approximated by F_{50}), the larger the amount of thermal energy (approximated by the GOES SXR). (Since F_{50} is a power-law normalization factor, it describes equally well the amount of nonthermal electrons of lower energies, which contain most of the nonthermal power.) Similar correlations have been reported before (see, *e.g.,* Battaglia, Grigis, and Benz, 2005, and references therein).

5. Summary and Conclusion

The following is a compilation of our results and can be used as a list of constraints for any flare and particle acceleration theories:

1. The total footpoint 50-keV flux correlates remarkably well with the GOES maximum 1 – 8 Å flux. The relationship is fairly linear.
2. There is no statistically significant difference in our sample between "leading" and "trailing" footpoints, as regards asymmetries.
3. Flares are mostly located at ± 15 degrees of solar latitude, and flare parameters have no marked longitudinal dependence.
4. Spherical separation between footpoints seems not to correlate with any of the other parameters examined, with the surprising exception of HXR burst duration, where a weak correlation was found. This seems to indicate that longer loops produce longer HXR peaks, probably because the magnetic disturbance and particle acceleration last longer in long loops than in short ones.
5. Flare footpoint spectral indices γ are seldom below ≈ 2.4 (1 case out of 172). "Peak Times" are generally harder than "Whole Peak" intervals, a natural consequence of the commonly observed soft – hard – soft behavior of flares.
6. Approximately 25% ("Peak Times") to $\approx 40\%$ ("Whole Peaks") of double footpoint flares have spectral index differences $\Delta\gamma$ consistent with zero. $\Delta\gamma$ can reach 0.6, and only rarely goes beyond. The amplitude of $\Delta\gamma$ is uncorrelated with flare GOES class.
7. The 50-keV footpoint flux ratios are never quite unity, are typically between 1 and 2, and only seldom go beyond 3. This result could be due to observational bias.
8. The asymmetric loop model, where a column density difference is responsible for the difference in spectral index and flux between HXR footpoints, cannot explain a majority of our observations. It is therefore not a dominant factor.

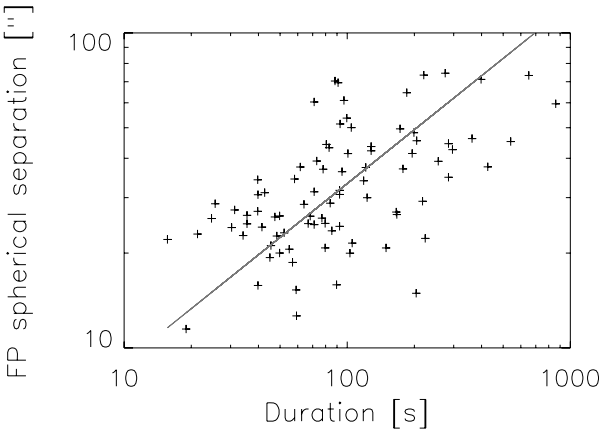

Figure 8 "Whole Peak" duration versus footpoint separation. The error bars are small and were not omitted. The gray line is a linear fit (using the bisector method) to the data. It yields a power-law slope of 0.6 ± 0.1.

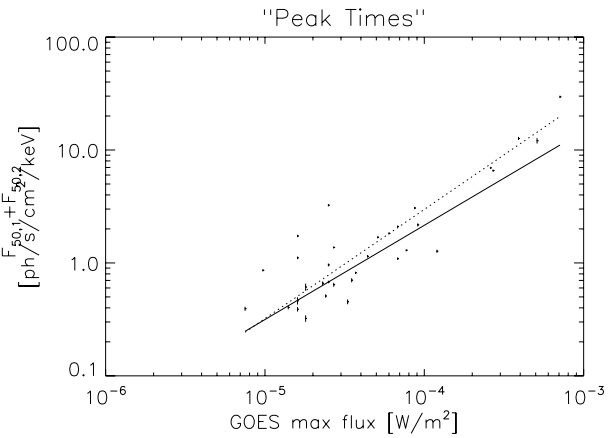

Figure 9 GOES maximum flux in the 1 – 8 Å band versus peak 50-keV flux of both footpoints, with 1-σ errors. The solid line is a power-law linear fit to the data. The dotted line is another power-law fit to the data, using the bisector method.

9. The greatest asymmetry being around "Peak Times" further suggests that magnetic reconfiguration is greatest at those times.

Acknowledgements This work could not have been completed without Swiss National Science Foundation (SNSF) Grant No. PBEZ2-108928, NASA Heliospheric Guest Investigator Grant No. NNX07AH74G, and NASA Contract No. NAS 5-98033. We would also like to thank the anonymous referees for their useful comments.

Appendix A: Column Density Effects in Asymmetric Loops

Figures 10 and 11 show the numerically computed effect of loop asymmetry on the 50-keV component of the thick-target bremsstrahlung spectra produced by two identical accelerated electron distributions. Notice that emission at the footpoint of the leg of the loop with the least column density is softer than the other one but has more flux.

Increasing δ increases all three parameters ($\Delta\gamma$, $F_{50,\mathrm{r}}$, and coronal/FP flux), whereas increasing f only increases the first two, and makes the last one decrease. Hence, to have large $\Delta\gamma$ and for the spatially extended coronal flux to be lost within the dynamic range of the instrument, a high f (*i.e.*, loop asymmetry) is required.

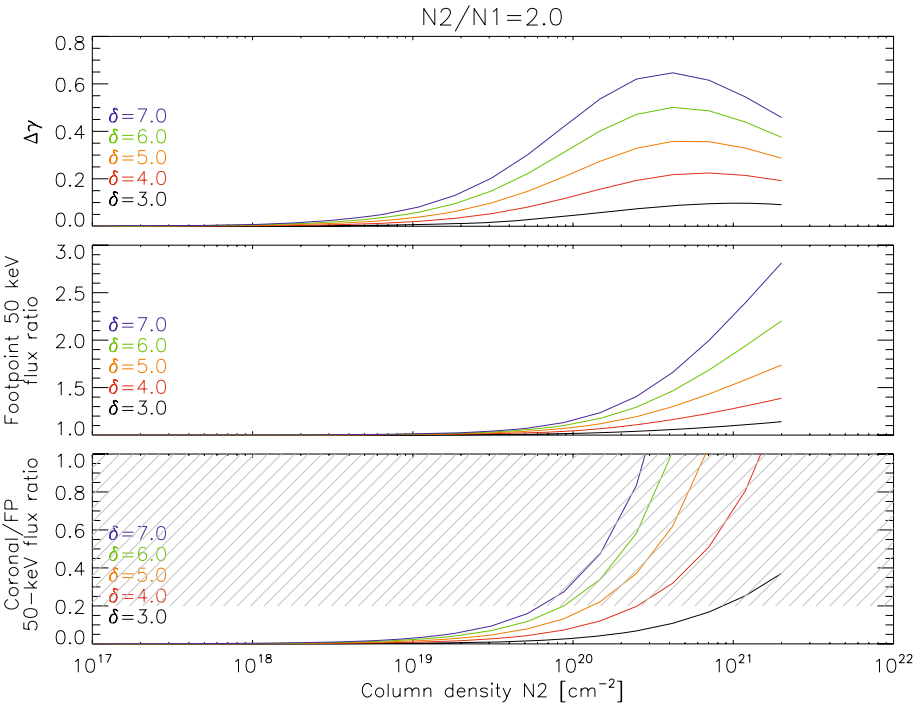

Figure 10 If identical accelerated electron distributions travel through two different column densities $N1$ and $N2$ (such as would be the case in an asymmetric loop), then the bremsstrahlung photon spectra they will emit at each footpoint will be slightly different. Top: Spectral index difference $\Delta\gamma = \gamma_1 - \gamma_2$ between footpoint spectra, assuming $N2 = 2 \times N1$. Middle: 50-keV flux ratio $F_{50,r} = \frac{F_{50,1}}{F_{50,2}}$ between footpoints. Bottom: Ratio of the total 50-keV flux present in the corona to that present in both footpoints. The footpoint spectral indices and 50-keV fluxes were determined by fitting a power-law in the 25 – 75 keV band, typical of the observations presented in this paper. The hatched part indicates areas where 50-keV coronal emission would be observed, assuming a conservative dynamic range of 5 for the instrument. δ is the accelerated electron power-law spectral index.

Figure 12 show the same data as Figures 10 and 11, but with different axes. The bottom plot of Figure 12 clearly shows that, for a hard flare (such as we have in this study) to have a flux ratio beyond 2 (or smaller than 1/2), and have the coronal part of the thick-target 50-keV flux go unobserved, unreasonable values for f (beyond 10!) or $N2$ would have to be considered. In the trap + precipitation model, the footpoint with the highest (in altitude) mirror point will stop only the lowest energy electrons. All the high-energy electrons will mostly stop (and emit bremsstrahlung) in the other footpoint. In this case, the footpoint with the hardest emission will also have the most flux.

Appendix B: RHESSI Imaging Spectroscopy Errors

Errors in RHESSI imaging spectroscopy are extremely difficult to estimate, as each individual pixel or feature in an image is heavily correlated to other parts of the image, via the point-spread function.

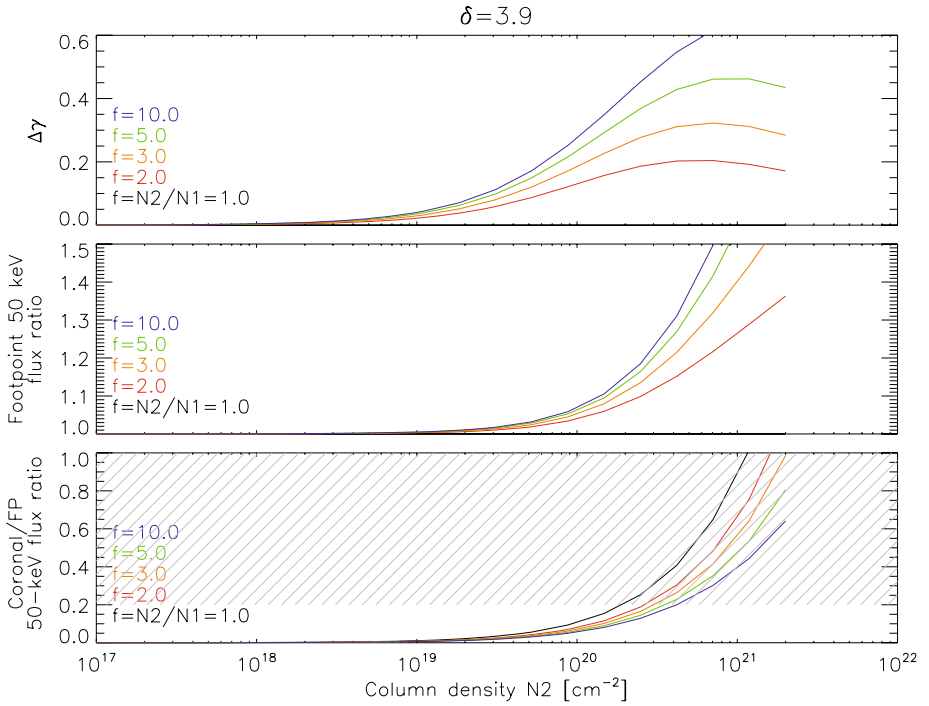

Figure 11 Similar results as for Figure 10, except that the ratio $f = N2/N1$ was varied and δ has been maintained constant at 3.9.

The current heuristic method implemented in OSPEX, the standard RHESSI imaging spectroscopy software package, is to define the error on the flux of a feature as the maximum of the flux outside of the (visually selected) sources, divided by a somewhat arbitrary value f $n = 3$. When the data are very noisy (*e.g.,* images made at high energies, where the counts are low), this method will assuredly underestimate the errors. This later point is not an issue for our study, though, as we have discarded noisy images with our choice of energy bands.

We have tried another method, similar to Mitani (2005), where a Gaussian is fitted to a histogram of the pixel values of the whole image. The error on a source flux is then taken to be the 1-σ extent of this distribution, multiplied by the number of pixels in that source. We have labeled that method "Gaussian Background."

To estimate the accuracy of each method's error estimation, we have plotted the histogram of the normalized residuals of all our spectral fittings (see Figure 13). If we assume our power-law model to be correct, then the leftmost plot of Figure 13 leads us to conclude that errors in the standard OSPEX imaging spectroscopy package are typically overestimated by a factor ≈ 2. We then chose $n = 6$ as our heuristic number, obtaining the plot in the middle of Figure 13, where a fitted Gaussian has σ very close to unity. This is the scheme that we finally settled upon.

The fitting parameters hardly change whether we choose to use OSPEX with $n = 3$ or 6, or with the Gaussian background method; only the 1-σ error on those parameters are influenced by the choice of the method. Moreover, the results and conclusions obtained by

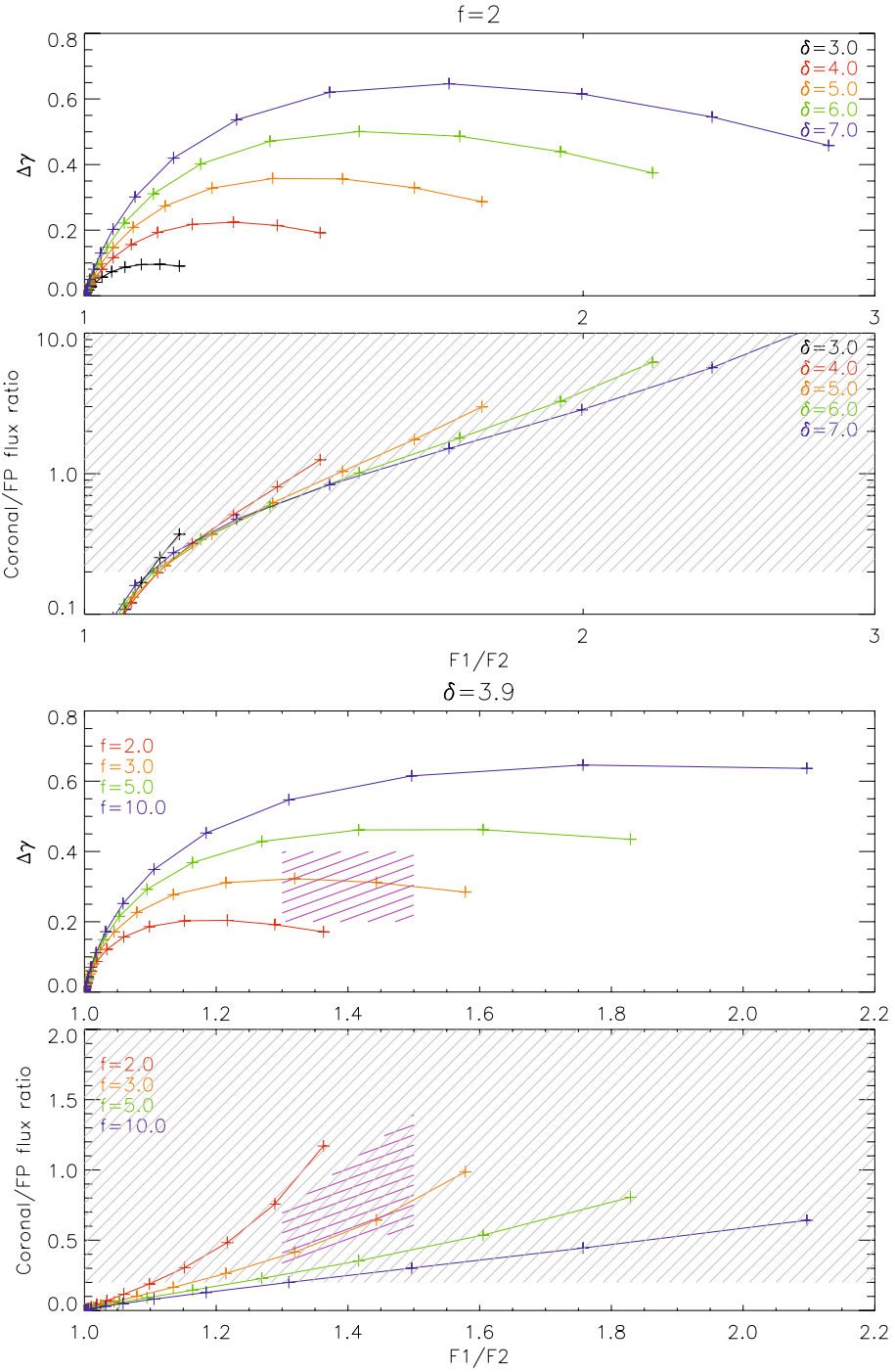

Figure 12 $\Delta\gamma$ and $F_{50,\mathrm{r}}$ for increasing $N2$. $N2$ varies from 0 (leftmost point) to 2×10^{21} cm^{-2} (rightmost point). The purple shaded region in the third plot is the range of values for the 23 July 2002 event. It has been roughly mapped to the fourth plot.

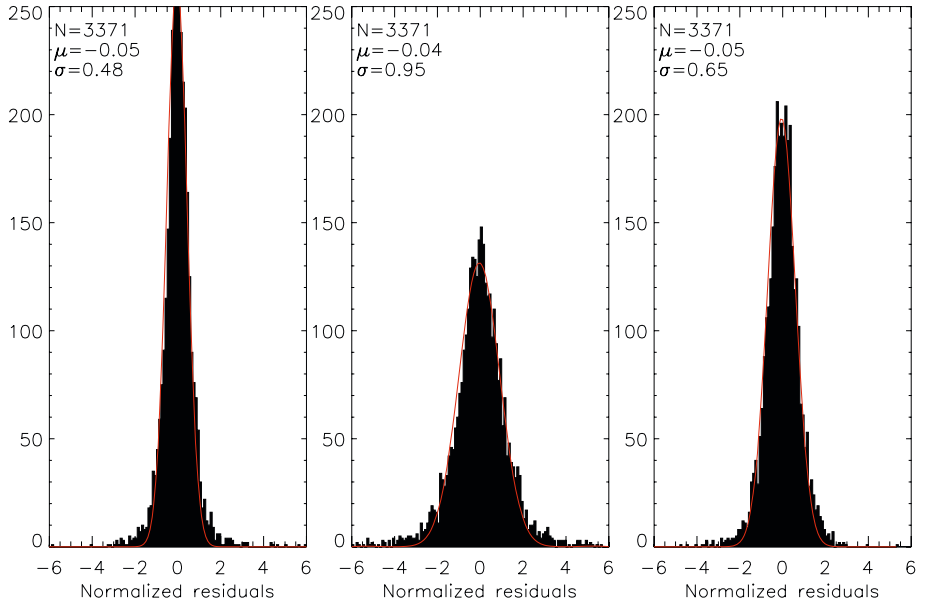

Figure 13 Histograms of normalized residuals: OSPEX with $n = 3$ (left), OSPEX with $n = 6$ (middle), and Gaussian background method (right). N is the total number of data points fitted, μ and σ the mean and standard deviation, respectively, of the Gaussians fitted to the histograms.

using either the OSPEX with $n = 6$ or the Gaussian background method do not change significantly.

References

Aschwanden, M.J., Fletcher, L., Sakao, T., Kosugi, T., Hudson, H.: 1999, *Astrophys. J.* **517**, 977.
Bai, T., Ramaty, R.: 1978, *Astrophys. J.* **219**, 705.
Battaglia, M., Benz, A.O.: 2006, *Astron. Astrophys.* **456**, 751.
Battaglia, M., Grigis, P.C., Benz, A.O.: 2005, *Astron. Astrophys.* **439**, 737.
Brown, J.C.: 1971, *Solar Phys.* **18**, 489.
Brown, J.C.: 1973, *Solar Phys.* **28**, 151.
Dennis, B.R.: 1985, *Solar Phys.* **100**, 465.
Emslie, A.G., Kontar, E.P., Krucker, S., Lin, R.P.: 2003, *Astrophys. J.* **595**, L107.
Grigis, P.C., Benz, A.O.: 2004, *Astron. Astrophys.* **426**, 1093.
Holman, G.D., Sui, L., Schwartz, R.A., Emslie, A.G.: 2003, *Astrophys. J.* **595**, L97.
Hoyng, P., Duijveman, A., Boelee, A., de Jager, C., Galama, M., Hoekstra, R., Imhof, J., Lafleur, H., Machado, M.E., Fryer, R.: 1981, *Astrophys. J.* **244**, L153.
Hurford, G.J., Schmahl, E.J., Schwartz, R.A., Conway, A.J., Aschwanden, M.J., Csillaghy, A., Dennis, B.R., Johns-Krull, C., Krucker, S., Lin, R.P., McTiernan, J., Metcalf, T.R., Sato, J., Smith, D.M.: 2002, *Solar Phys.* **210**, 61.
Isobe, T., Feigelson, E.D., Akritas, M.G., Babu, G.J.: 1990, *Astrophys. J.* **364**, 104.
Kašparová, J., Karlický, M., Kontar, E.P., Schwartz, R.A., Dennis, B.R.: 2005, *Solar Phys.* **232**, 63.
Kontar, E.P., Brown, J.C., McArthur, G.K.: 2002, *Solar Phys.* **210**, 419.
Krucker, S., Lin, R.P.: 2002, *Solar Phys.* **210**, 229.
Lin, R.P., Dennis, B.R., Hurford, G.J., Smith, D.M., Zehnder, A., Harvey, P.R., *et al.*: 2002, *Solar Phys.* **210**, 3.

Masuda S.: 1994, Hard X-ray sources and the primary energy release site in solar flares. Ph.D. thesis, University of Tokyo.
Melrose, D.B., Brown, J.C.: 1976, *Mon. Not. Roy. Astron. Soc.* **176**, 15.
Neupert, W.M.: 1968, *Astrophys. J.* **153**, L59.
Petrosian, V., Donaghy, T.Q., McTiernan, J.M.: 2002, *Astrophys. J.* **569**, 459.
Saint-Hilaire, P., Benz, A.O.: 2002, *Solar Phys.* **210**, 287.
Saint-Hilaire, P., Benz, A.O.: 2005, *Astron. Astrophys.* **435**, 743.
Sakao T.: 1994, Characteristics of solar flare hard X-ray sources as revealed with the hard X-ray telescope aboard the *Yohkoh* satellite. Ph.D. thesis, University of Tokyo.
Schmahl, E.J., Pernak, R.L., Hurford, G.J., Lee, J., Bong, S.: 2007, *Solar Phys.* **240**, 241.
Schwartz, R.A., Csillaghy, A., Tolbert, A.K., Hurford, G.J., Mc Tiernan, J., Zarro, D.: 2002, *Solar Phys.* **210**, 165.
Smith, D.M., Lin, R.P., Turin, P., Curtis, D.W., Primbsch, J.H., Campbell, R.D., Abiad, R., *et al.*: 2002, *Solar Phys.* **210**, 33.
Zharkova, V.V., Gordovskyy, M.: 2006, *Astrophys. J.* **651**, 553.